Supporting Information

McCoy and Hubbell 10.1073/pnas.1017877108

SI Text

Microscopic Order Macroscopic Disorder (MOMD) Simulations of Continuous Wave (CW)-EPR Spectra and Determination of $K(P)$. Experimental spectra were fit using a Labview™ interface of the program NLSL developed by Freed and coworkers (1, 2). The software is available upon request (caltenba@ucla.edu). The program performs a least-squares fit of the user-defined spectral parameters using Levenberg–Marquardt (LM), simplex, or Monte Carlo–based algorithms. Typically, a combination of simplex and LM was used. Because of the large number of parameters in a typical MOMD simulation, it was important to define a model and constrain certain parameters to physically realistic values. For all fits, the values for the **A** and **g** magnetic tensors were fixed as $g_{xx} = 2.0078$, $g_{yy} = 2.0058$, $g_{zz} = 2.0022$, and $A_{xx} = 6.2$, $A_{yy} = 5.9$, $A_{zz} = 37.0$, which are experimental values corresponding to R1 in an aqueous environment (3). The $\log_{10}$ of the three components of the rotational diffusion tensor of the nitroxide are given in a modified spherical form as

$$\bar{R} = \frac{1}{3}(R_x + R_y + R_z), \qquad N = R_z - \frac{(R_x + R_y)}{2},$$
$$N_{xy} = R_x - R_y,$$

where R_x, R_y, and R_z are the principle components of the rotational diffusion tensor in Cartesian form (in s^{-1}). For data simulated in this work, axial symmetry was assumed, which implies $N_{xy} = 0$. In addition to the rotational diffusion parameters, models of anisotropic motion require a restoring potential defined in general by the following expression:

$$U(\Omega) = -k_B T \sum_{L,K} c_K^L D_{0K}^L(\Omega),$$

where the terms $D_{0K}^L(\Omega)$ and c_K^L represent a series of spherical harmonics and their weighting coefficients, respectively. The symmetry axis of U defines the coordinates of the protein reference frame from which anisotropic motion can be interpreted. $\Omega = (\alpha,\beta,\gamma)$ are the angles relating the axes of the diffusion tensor to this frame. Diffusion tilt angles were fixed to either $(\alpha,\beta,\gamma) = (0,36°,0)$ or $(\alpha,\beta,\gamma) = (0,90°,36°)$ for z-axis or x-axis anisotropy, respectively. The reported order parameter S can be directly calculated from the weighting coefficients of the restoring potential (2). The reported correlation time τ was calculated from:

$$\tau = \frac{1}{(6 \times 10^{\bar{R}})}.$$

Having a series of data from the same spin-labeled protein at different pressures provided a unique advantage in spectral simulations. As such, a global fitting strategy was employed. One- and two-component fits were performed as indicated on data from multiple pressures to find the best parameters for the weighting coefficients of the restoring potential. When a good parameter was found for all pressures, it was fixed. This reduced the number of fit parameters in the rest of the pressure data to iterations of the parameters N and $\bar{R}$ and relative populations where a two-component fit was needed. Removing the constraint from the restoring potential did not greatly improve the quality fits and often lead to physically unrealistic results in rate parameters.

MOMD Simulations of 82R1 and 80R1. Figs. S1 and S2 show overlays of the single-component fits of the experimental data of 82R1 and 80R1, respectively, along with the calculated correlation time τ and order parameter S at each pressure. For the anisotropic motion typically found for R1 at solvent-exposed helical sites, changes in the central linewidth reflects primarily changes in rate and not order of motion (4). The central linewidths of 80R1 and 82R1 change substantially with pressure, and thus the rates are clearly changing. It was found that a variable rate with fixed order at the values indicated in the figures provided fits that were not significantly improved by allowing variations in order as well. This is a physically realistic model, because the transition state has larger volume (thus changing rate with pressure), but the amplitude (order) of the motion for noninteracting states should not be strongly pressure dependent at low pressures.

MOMD Simulations of 44R1. For 44R1, a two-component fit was required. The mobile component was treated as previously described, having simple anisotropic motion defined by a correlation time τ and an order parameter S. The second immobile component was assumed to have isotropic motion dominated by the rotational diffusion of the protein. Accordingly, the immobile component of a two-component simulation was constrained by $N = N_{xy} = 0$. Fig. S3A shows the results of the two-component fits of 44R1 and the relative populations of immobile and mobile components at each pressure. Also shown is the plot of $\ln(\tau/\tau_0)$ versus pressure for the mobile component (Fig. S3B). As shown, the plot is linear, and the slope provides the activation volume shown. Fig. S3C shows the pressure-dependent spectral changes of 44R1 in both the WT* and cross-linked (21C/142C) background of T4L (see *Methods*).

Subtraction Analysis of 44R1. The mutant 44R1/E45A, consists largely of one component (*m*) at all pressures studied. This provided EPR spectra corresponding to the pressure dependence of a nearly pure *m* state, which could then be subtracted from the spectra of 44R1 at the same pressure to provide the relative populations and $K(P)$ without invoking spectral simulations. *Panels 1* and *2* (Fig. S4A) contain the data from 44R1 and 44R1/45A, respectively, obtained at various pressures all normalized to the same number of spins. *Panel 3* shows the result of a spectral titration where *Panel 2* spectra are subtracted from the corresponding spectra of *Panel 1*; the endpoint was judged by spurious features that occur with oversubtraction. *Panel 3* also shows the estimated fraction of immobile component at each pressure determined from the titration. The poor quality of the $P = 0$ subtraction (*Panel 3*, black trace) is a reflection of the approximations made in the model (i.e., that the mobile states from 44R1 and 44R1/45A are precisely identical). However, the point to be made is that the $\ln[K/K_0]$ versus pressure plots (Fig. S4B) for both methods (subtraction or MOMD) are in reasonable agreement. In either case, the data support the model that pressure favors an interaction with the neighboring glutamate residue in 44R1 because of the smaller molar volume of the complex.

MOMD Simulations of 118R1 in 8 M and 2 M Urea. For 118R1 in 8 M urea the data was well fit to a single component assuming simple isotropic motion. The single component of the simulation was constrained by $N = N_{xy} = 0$, and only the average rate parameter ($\bar{R}$) was varied. Fig. S5A shows overlays of the single-component fits of the experimental data of 118R1 in 8 M urea along with the calculated τ at each pressure. Also shown is the plot of $\ln(\tau/\tau_0)$

versus pressure for the single component (Fig. S5B); the plot is again linear, and the slope provides the activation volume shown.

For 118R1 in 2 M urea a two-component fit was required. Both the mobile and immobile components were treated as having simple isotropic motion. In the case of the mobile component, the isotropic motion is assumed to arise from the rapid exchange of a random coil, and in the case of the immobile component, the motion is dominated by the rotational diffusion of the protein. Accordingly, both components were constrained by $N = N_{xy} = 0$. Fig. S5C shows the results of the two-component fits of 118R1 in 2 M urea and the relative populations and rate constants of the immobile and mobile components at each pressure.

MOMD Simulations of 46R1. For 46R1 two-component fits were also required; like 118R1 in 2 M urea, the spectra were adequately fit with two isotropic components. Both the mobile and immobile component were constrained by $N = N_{xy} = 0$. Fig. S6 shows the results of the two-component fits of 46R1 and the relative populations and correlation times of the immobile and mobile components at each pressure.

Viscosity at Increasing Pressures. The contribution of motion to the EPR spectra of spin-labeled proteins provides the richest source of protein structural data in an SDSL experiment. As such, it is important to account for all sources of motion reported in the EPR lineshape. In most CW-EPR experiments, a viscosity agent is added to sample solutions to damp out the contributions to motion arising from protein rotary diffusion. Based on the Stokes–Einstein equation, this selectively affects protein rotary diffusion and not the internal motions of the R1 side chain because the magnitude of the effect of the viscogen scales with the size of the diffusing species (5). In the experiments described in this communication, all samples were measured in 20 mM MES and water solutions (pH 6.8) containing ~25–30% wt/vol of a high viscosity agent (either sucrose of Ficoll-70). Under pressure, the viscosity of the sample solution will change because of competing effects. Water as the main component of the solution has been previously studied; at 20 °C, the relative viscosity of water decreases at low pressure (to 1 kbar) and increases by approximately 15% from 1–4 kbar (6). However, because water is a compressible liquid, the sample volume will decrease under pressure, and as a consequence, the concentration of both the protein and the viscogen will also increase. As such, it is important to address the contributions to nitroxide motion due to viscosity changes with pressure on both (*i*) protein rotary diffusion and (*ii*) the microenvironment experienced by R1.

Effects of Pressure on Protein Rotary Diffusion. To assess the contribution of changing viscosity with pressure on protein rotary diffusion, a diphenyl substituted derivative of the R1 nitroxide [R(2f)] (Fig. S7A) was employed. The sterically hindered nitroxide side chain has been shown previously to be rigidly attached to the protein and serves as a direct monitor of protein rotational diffusion rate (5, 7). As in earlier experiments using R(2f) to measure rotary diffusion of T4L, site 72 was selected (5).

Fig. S7A shows spectra of 72R(2f) in 20 mM MES buffer alone or buffer containing either 25% wt/vol Ficoll-70 or 30% wt/vol sucrose as indicated. In each case, the splitting of the hyperfine extrema ($2A'_{zz}$) is well resolved and increases with pressure. The rotational correlation times were easily obtained from one-component fits assuming isotropic motion. The increase in rotational correlation times (i.e., decrease in rotational rate) is plotted as a function of pressure in Fig. S7B.

Effects of Viscosity on the R1 Microenvironment. To test the effects of increasing solvent microscopic viscosity on R1 side-chain motion, 80R1 spectra were recorded in water and D_2O solutions. The in-

crease in viscosity of D_2O versus water is approximately 25%. 80R1 was chosen because its internal motion is comparatively fast and sensitive to small changes in motion. As shown in Fig. S7C the CW-EPR spectra of 80R1 in water versus D_2O are superimposable. Because of the small size of the nitroxide side chain, changes in viscosity with increasing pressure will affect protein rotary diffusion only and will not affect the internal motion of R1 on the time scale of X-band EPR (5).

CD Characterization of Destabilized Mutants of T4L. To explore the pressure response of protein conformational equilibria as detected by SDSL, T4L was specifically destabilized by introducing R1 at partially buried (118R1) or buried (46R1) sites in the structure. To characterize these mutants with regard to overall secondary structure and tertiary fold, CD denaturation curves were measured at pH 6.8. Shown in Fig. S8 are the normalized denaturation curves based on the absorption of circularly polarized light at 223 nm in the WT* (black trace), 118R1 (green trace), and 46R1 (red trace) derivatives of T4L as a function of urea concentration. It is apparent from these data that the stability of both mutants is decreased relative to the WT* T4L. We calculate a ΔG_{H_2O} of 118R1 is approximately 11.6 kcal/mol, approximately 1.5 kcal/mol below that measured for the WT* (approximately 13.1 kcal/mol). The lack of steepness of the denaturation curve of 46R1 is of particular interest. Steepness of the denaturation curve (or *m* value) is related to the cooperativity of the unfolding reaction (8); It has been noted that in cases where unfolding intermediates exist, the steepness of the urea denaturation curve will decrease (9). Fits of the data from 46R1 to a two-state model predict a ΔG_{H_2O} of approximately 4.9 kcal/mol; underestimates of ΔG_{H_2O} have also been reported to be consistent with multistate unfolding (9). One explanation for the above result is that the N domain of the protein is substantially destabilized by the spin label at site 46R1; the intermediate state is likely the unfolded N domain and a folded, native-like C domain. This particular intermediate state has been suggested by others (10, 11).

CD experiments were conducted on a Jasco-810 spectropolarimeter. Samples consisting of 0.5 mg/mL protein in 5 mM MES (pH 6.8) at various urea concentrations were measured in a quartz curvette (1-mm path length). Urea solid was obtained commercially (Sigma) and was of the highest purity. Sample urea solutions were made fresh and allowed to rest at room temperature for 24 h before data collection. Ellipticity was monitored at 223 nm. Denaturation curves were fit to a two-state transition model (12) by a nonlinear least-squares procedure.

Hydrostatic Pressure Generation. A high-pressure cell was adapted for EPR use from the high-pressure NMR cell design of Yonker and coworkers (13). Lengths of polytetrafluoroethylene (PTFE)-coated fused silica capillary were obtained commercially (Polymicro Technology). The small capillary tubes are extruded from larger stock and coated with PTFE at the factory. Extruding the material removes all small fissures and irregularities from the surface of the capillary tubes, and the application of a protective layer of PTFE ensures that the integrity of the surface remains high. The integrity of the fused silica surface is important to obtain maximum tensile strength for high-pressure applications (14). The inner and outer diameter of the capillary was chosen to maximize tensile strength and the filling factor available for sample. The maximum pressure that a cylindrical cell can withstand can roughly be approximated by an elastic cylinder model (14):

$$P_{\max} = \sigma_T \left[\left(\frac{d_o}{d_i} \right)^2 - 1 \right] \left[\left(\frac{d_o}{d_i} \right)^2 + 1 \right]^{-1},$$

where σ_T represents the tensile strength of the material and d_o and d_i are outer and inner diameters, respectively. We found the mini-
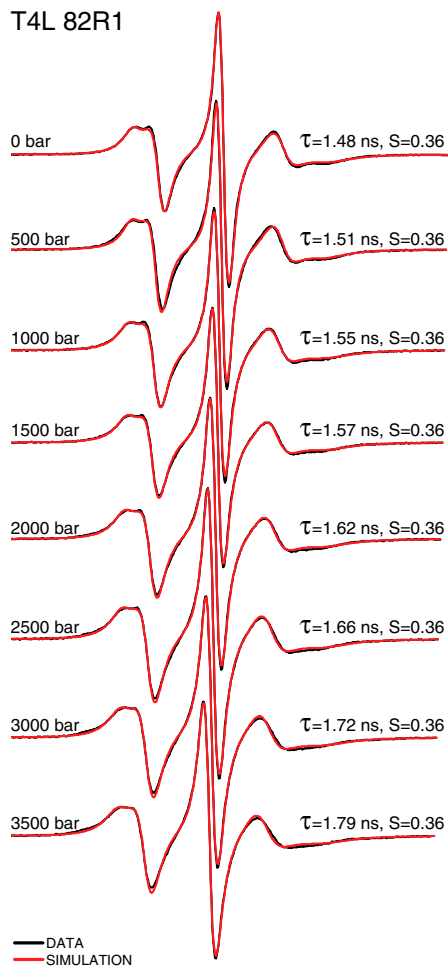
mum ratio of 3:1 outer to inner diameter to be sufficient for regular use at pressures up to 4 kbar. Capillaries with an o.d.:i.d. ratio of 360:100 μm were used because they were standard from the manufacturer.

Long lengths of PTFE-coated capillaries were bent back and forth with a jewelers torch so that several hairpin bends (typically between 15 to 25) were created. During the creation of the sample bundle, PTFE was effectively removed from each bend. Exposed areas of tube were dipped in a solution of 50% ethyl ether, 50% ethanol containing dissolved parlodion (~1 g per 200 mL). After solvent evaporation, a protective coat of parlodion remained on the exposed areas of the sample bundle. One end of the sample bundle was bonded to a center-drilled copper plug (Fig. S9*B*) with epoxy (EcoBond 104) and heat cured. Samples were loaded with a syringe through the copper plug using a homebuilt syringe adapter. Once filled, the remaining
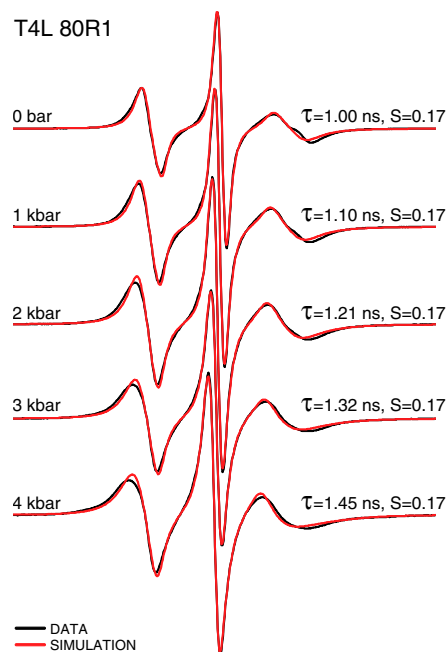
end of the cell was flame sealed. The sample bundle was then placed in a standard 5-mm-diameter NMR tube for use in the spectrometer (Fig. S9*A*). All elements of the high-pressure apparatus are shown in Fig. S9.

Pressure generation was accomplished with either a hand-operated syringe pump (High-Pressure Equipment Model 37-5.75-60) rated at 60 kpsi (4.14 kbar) or with an automated air-to-water pressure intensifying unit (Pressure BioSciences Model HUB440) rated at 55 kpsi (3.79 kbar). Initial data collection was performed exclusively with the hand-operated pump. After upgrading to the automated pressure generation system (HUB 440), we found that the robustness of our sample bundles was greatly increased. It may be that with the air-to-water intensifier the more gradually applied pressure may decrease stress on the sample bundle.

1. Schneider DJ, Freed JH (1989) *Biological Magnetic Resonance*, eds Berliner LJ, Reuben J (Plenum, New York), Vol 8, pp 1–76.
2. Budil DE, Saxena S, Freed JH (1996) Nonlinear-least-squares analysis of slow motional EPR spectra in one and two dimensions using a modified Levenberg–Marquardt algorithm. *J Magn Reson Ser A* 120:155–189.
3. Kusnetzow AK, Altenbach C, Hubbell WL (2006) Conformational states and dynamics of rhodopsin in micelles and bilayers. *Biochemistry* 45:5538–5550.
4. Columbus L, Hubbell WL (2004) Mapping backbone dynamics in solution with site-directed spin labeling. *Biochemistry* 43:7273–7287.
5. Lopez CJ, Fleissner MR, Guo Z, Kusnetzow AK, Hubbell WL (2009) Osmolyte perturbation reveals conformational equilibria in spin-labeled proteins. *Protein Sci* 18:1637–1652.
6. Bett KE, Cappi JB (1965) Effect of pressure on the viscosity of water. *Nature* 207:620–621.
7. Sale K, Sar C, Sharp KA, Hideg K, Fajer PG (2002) Structural determination of spin label immobilization and orientation: Monte Carlo minimization approach. *J Magn Reson* 156:104–112.
8. Myers JK, Pace CN, Scholtz JM (1995) Denaturant *m* values and heat capacity changes: Relation to changes in accessible surface areas of protein folding. *Protein Sci* 4:2138–2148.
9. Pace CN (1986) Determination and analysis of urea and guanidine hydrochloride denatiration curves. *Methods Enzymol* 131:266–280.
10. Llinas M, Marqusee S (1998) Subdomain interactions as a determinant in the folding and stability of T4 lysozyme. *Protein Sci* 7:96–104.
11. Llinas M, Gillespie B, Dahlquist FW, Marqusee S (1999) The energetics of T4 lysozyme reveal a hierarchy of conformations. *Nat Struct Biol* 6:1072–1078.
12. Pace CN, Shaw KL (2000) Linear extrapolation method of analyzing solvent denaturation curves. *Proteins Suppl* 4:1–7.
13. Pfund DM, Zemanian TS, Linehan JC, Fulton JL, Yonker CR (1994) Fluid structure in supercritical xenon by nuclear magnetic resonance spectroscopy and small angle X-ray scattering. *J Phys Chem* 98:11846–11857.
14. Yamada H, et al. (2001) Pressure-resisting cell for high-pressure, high-resolution nuclear magnetic resonance measurements at very high magnetic field. *Rev Sci Instrum* 72:1463–1471.
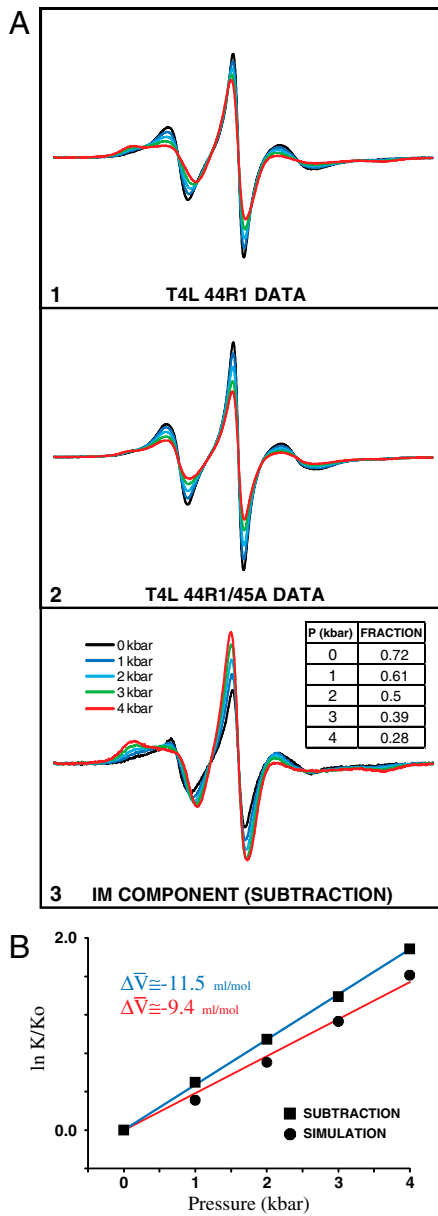
T4L 82R1

0 bar τ=1.48 ns, S=0.36

500 bar τ=1.51 ns, S=0.36

1000 bar τ=1.55 ns, S=0.36

1500 bar τ=1.57 ns, S=0.36

2000 bar τ=1.62 ns, S=0.36

2500 bar τ=1.66 ns, S=0.36

3000 bar τ=1.72 ns, S=0.36

3500 bar τ=1.79 ns, S=0.36

—— DATA
—— SIMULATION

Fig. S1. Experimental (black trace) and simulated (red trace) EPR spectra for T4L 82R1 at the indicated pressure. For each, the correlation time τ and order parameter S determined by simulation are provided.

T4L 80R1

0 bar τ=1.00 ns, S=0.17

1 kbar τ=1.10 ns, S=0.17

2 kbar τ=1.21 ns, S=0.17

3 kbar τ=1.32 ns, S=0.17
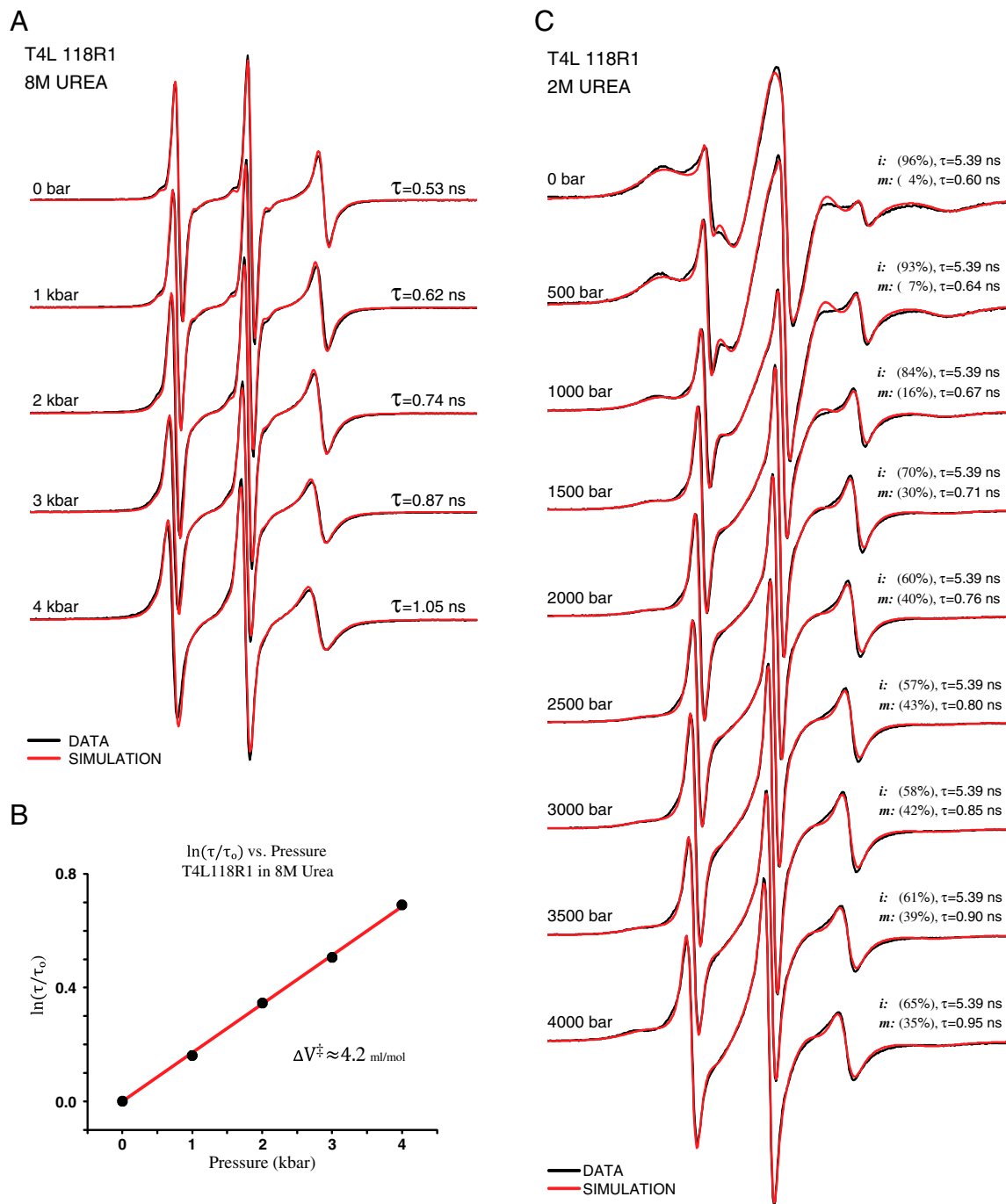
4 kbar τ=1.45 ns, S=0.17

—— DATA
—— SIMULATION

Fig. S2. Experimental (black trace) and simulated (red trace) EPR spectra for T4L 80R1 at the indicated pressure. For each, the correlation time τ and order parameter S determined by simulation are provided.

A

T4L 44R1

0 bar
  i: (29%), τ=5.67 ns
  m: (71%), τ=2.00 ns, S=0.24

1 kbar
  i: (35%), τ=6.28 ns
  m: (65%), τ=2.17 ns, S=0.24

2 kbar
  i: (45%), τ=6.75 ns
  m: (55%), τ=2.32 ns, S=0.24

3 kbar
  i: (55%), τ=7.12 ns
  m: (45%), τ=2.45 ns, S=0.24

4 kbar
  i: (67%), τ=7.43 ns
  m: (33%), τ=2.65 ns, S=0.24

— DATA
— SIMULATION

B $\ln(\tau/\tau_o)$ vs. Pressure
Mobile Component T4L44R1

$\Delta V^{\ddagger} \approx 1.7$ ml/mol

C

T4L 44R1

T4L 21C/142C/44R1

— 0 kbar
— 1 kbar
— 2 kbar
— 3 kbar
— 4 kbar

Fig. S3. High-pressure EPR analysis of T4L 44R1. (*A*) Experimental (black trace) and simulated (red trace) EPR spectra at the indicated pressure. The correlation time τ is given for the isotropic immobile (*i*) component, and both τ and the order parameter *S* are given for the anisotropic mobile (*m*) component. In addition, percent population is given for the two components. Values of τ, *S*, and the populations were determined from simulation. (*B*) The pressure dependence of the correlation time for the mobile component. (*C*) Pressure-dependent EPR spectra for T4L 44R1 and the corresponding mutant with a disulfide cross link between 21C and 142C.

Fig. S4. Experimental determination of the relative populations of immobile and mobile states for T4L 44R1. (*A*) EPR spectra for T4L 44R1 at the indicated pressures (*Panel 1*), EPR spectra for the mutant T4L44R1/45A at the indicated pressures (*Panel 2*), and EPR spectra of the immobile component obtained by spectral subtraction of the spectra in *Panel 2* from the corresponding spectrum in *Panel 1*. (*B*) The pressure dependence of the equilibrium constant $K = $ [immobile]/[mobile] determined by the subtraction method (blue) and spectral simulation (red).

Fig. S5. High-pressure EPR analysis of T4L 118R1. (*A*) Experimental (black trace) and simulated (red trace) EPR spectra of the protein in 8 M urea at the indicated pressure. (*B*) Pressure dependence of the correlation time for the protein in 8 M urea. (*C*) Experimental (black trace) and simulated (red trace) EPR spectra for the protein in 2 M urea.
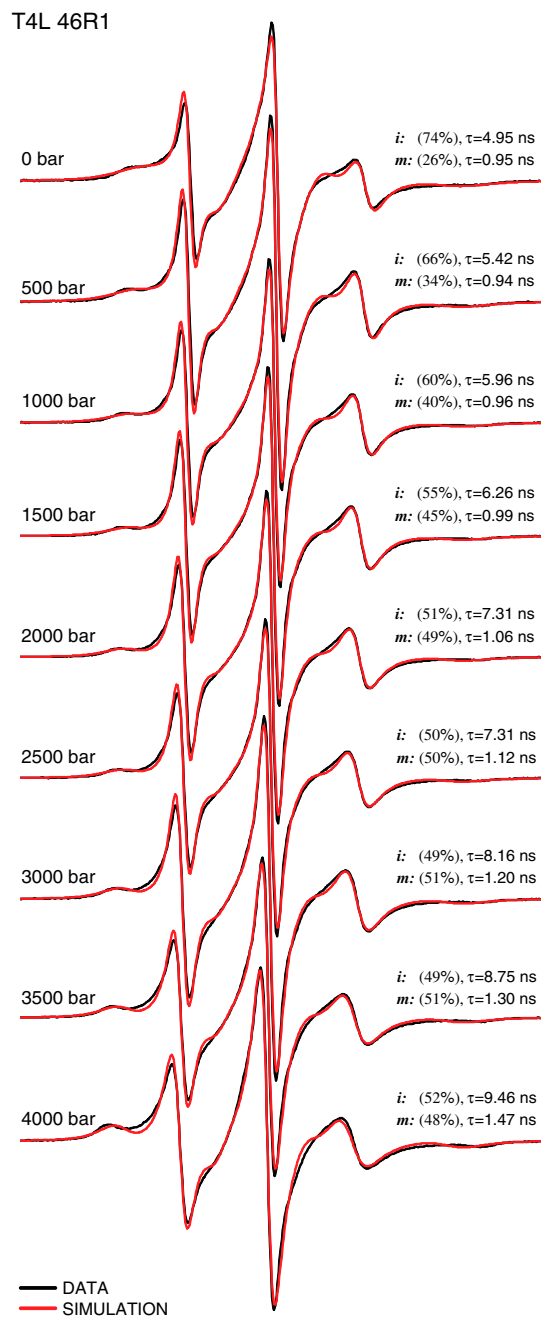
Fig. S6. High-pressure EPR analysis of T4L 46R1. Experimental (black trace) and simulated (red trace) EPR spectra at the indicated pressure. The correlation time τ is given for the isotropic immobile (*i*) component, and both τ and the order parameter S are given for the anisotropic mobile (*m*) component. The percent population is given for the two components. Values of τ, S, and the populations were determined from the simulation.
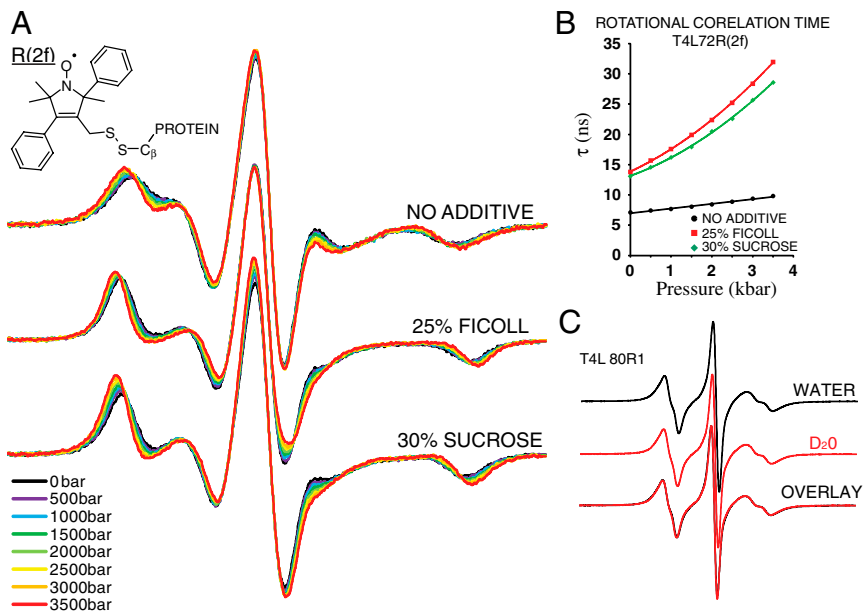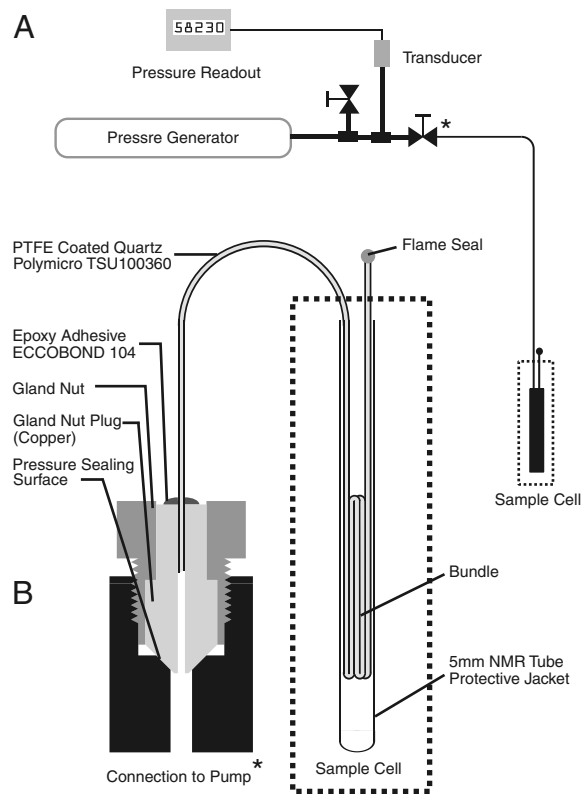
Fig. S7. The effect of pressure and viscous media on the rotational diffusion of T4L. (*A*) The EPR spectra of T4L 72R(2f) at the indicated pressure in buffer, 25% Ficoll, and 30% Sucrose. (*B*) The pressure dependence of the T4L rotational correlation time in each of the above media. (*C*) Comparison of EPR spectra of T4L80R1 in D_2O and water, each containing 25% Ficoll.
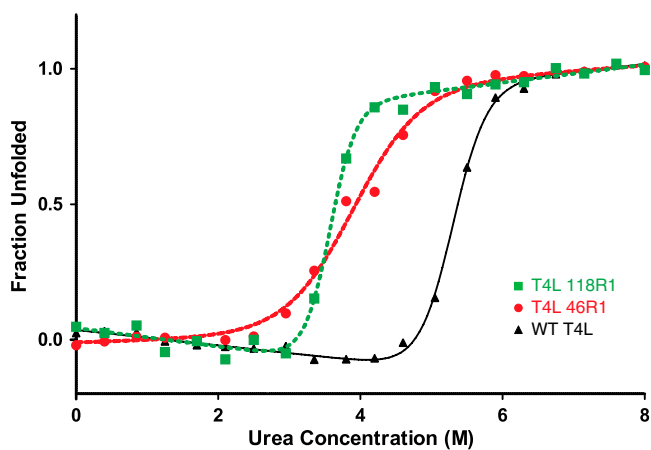
Fig. S8. Urea denaturation of native T4L and the indicated spin-labeled derivatives. The fraction unfolded was determined from circular dichroism measurements.

A

58230

Pressure Readout

Transducer

Pressre Generator

*

PTFE Coated Quartz
Polymicro TSU100360

Flame Seal

Epoxy Adhesive
ECCOBOND 104

Gland Nut

Gland Nut Plug
(Copper)

Pressure Sealing
Surface

Sample Cell

B

Bundle

5mm NMR Tube
Protective Jacket

Connection to Pump *

Sample Cell

Fig. S9. Schematic of the high-pressure EPR system. (*A*) Overview of the system. (*B*) Details of the high-pressure cell.